Volume 22
Number 5
4 February 2026
Pages 1073–1282

Soft Matter

rsc.li/soft-matter-journal

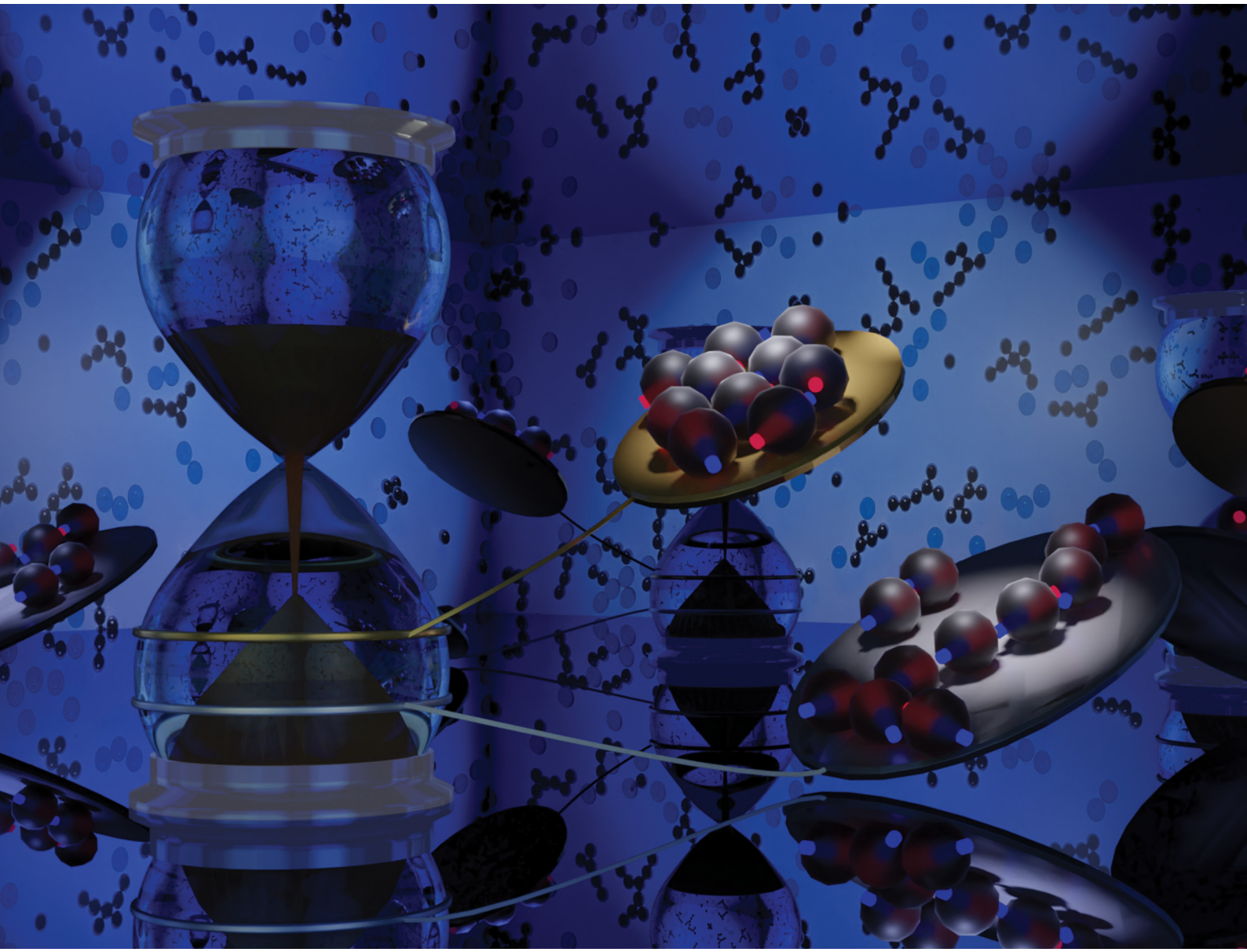

ISSN 1744-6848

ROYAL SOCIETY OF CHEMISTRY

PAPER
Ali Lakkis, Reinhard Richter, Sofia Kantorovich *et al.*
Two time scales drive the formation of transient networks in a ferrogranular experiment

Soft Matter

PAPER

View Article Online
View Journal | View Issue

Cite this: *Soft Matter*, 2026, **22**, 1081

Two time scales drive the formation of transient networks in a ferrogranular experiment

Ali Lakkis, *[a] Matthias Biersack, [a] Oksana Bilous, [b] Sofia Kantorovich [b] and Reinhard Richter *[a]

We are reporting experiments on the aggregation dynamics in a horizontally confined granular mixture composed of glass and magnetized steel spheres, under vertical vibration. Upon a sudden decrease of the shaking amplitude, magnetized particles undergo a transition from a dispersed to an aggregated state. For deep quenches, a transient, percolating network of magnetized spheres rapidly emerges and gradually coarsens into compact clusters. In contrast, moderate amplitude reductions lead directly to dense cluster formation without intermediate networking. Using structural and network metrics such as coordination number and its mean value, we identify two characteristic timescales: a fast one governing the head-to-tail chaining typical of dipolar hard spheres (DHS), and a slower one corresponding to the restructuring into compact aggregates. This progression is driven by the intrinsic susceptibility of the beads but is challenged by inter-sphere-friction. Thus, the employed susceptible dipolar hard spheres (SDHS) are a minimal model for phase separation with two intrinsic time scales in only one constituent.

Received 16th July 2025,
Accepted 7th November 2025

DOI: 10.1039/d5sm00726g

rsc.li/soft-matter-journal

1 Introduction

A ferrogranulate consists of numerous macroscopic bodies (grains or particles) that are either magnetized or possess significant susceptibility, enabling them to react sensitively to inherent or externally applied magnetic fields. While contact interactions are essential in standard granular materials,[1–3] in ferrogranulates, the influence of short- and long-range magnetic interactions may be even more significant. This is common ground with ferrofluids,[4] a suspension of magnetic nano-particles. Therefore, ferrogranulate can be seen as a connecting link between the latter two research topics (*cf.* Fig. 1). Indeed, the intriguing Rosensweig instability[5,6] has found a ferrogranular counterpart.[7] Moreover, in highly interacting ferrofluids, the formation of chains, rings, and loose networks of them is well known.[8–12] Similarly, chains and rings of magnetic beads have been studied in ferrogranulates.[13–16] Besides microstructural transitions, labyrinthine patterns have been observed in ferrofluids[4] and ferrogranulates.[17] Phase separation, already prominent in standard granulates, becomes more important due to the long-range interactions. Examples comprise phase separation in a 2D[18,19] and 3D[20] ferrogranular gas. During this process, in some cases compact clusters of spheres form immediately,[21] while in other cases transient networks, which are neither completely random, nor regular,[22] are a forerunner. Why and under what conditions can these networks be observed? We tackle this question in the present article, *i.e.* we elucidate the connection to the 4th node, sketched green in Fig. 1.

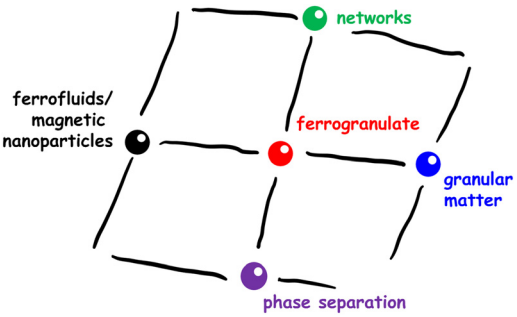

Fig. 1 Ferrogranulates are interconnecting four research topics.

Ferrogranular networks have been reported in a suspension of Ni-covered glass spheres,[23] in electromagnetically driven Ni-particles[14] as well as in colloidal suspensions within[24–27] or without[28] magnetic fields, or at interfaces.[29] A particularly "clean" example, put forward by Blair & Kudrolli,[30,31] is a mixture of mm-sized glass and magnetized steel beads produced with a high precision and monodispersity for ball bearings.[32,33] Starting from high shaker amplitude, Γ, for which a gas phase is observed, a deep quench in Γ gives rise to transient networks, which slowly coarsen to compact clusters. This coarsening dynamics was further studied in

[a] *Experimentalphysik V, University of Bayreuth, Universitätsstrasse 30, 95447 Bayreuth, Germany. E-mail: ali.lakkis@uni-bayreuth.de, reinhard.richter@uni-bayreuth.de*
[b] *Faculty of Physics, University of Vienna, Kolingasse 14-16, 1090 Vienna, Austria*

experiments and simulations,[34] which unveiled that the compaction to clusters takes place, because the magnetized beads are not simply dipolar hard spheres (DHS), but as well possess a considerable susceptibility. One may therefore call them susceptible dipolar hard spheres (SDHS).[35] Here the susceptibility acts as a "glue", which is working in all directions.[36,37] This observation was cast into a simple model, where the dipolar interaction is complemented by a central attraction[34,38] – a ferrogranular analogue to a Stockmayer fluid.[39] Note that without central attraction simulations cannot reproduce compact clusters, but just chains, rings or branched networks.[12,40]

The formation of transient networks appears to depend sensitively on the shaker amplitude, since for a shallow quench, compact clusters emerge at once,[30] and networks are not observed. So far, a systematic quantification of the coarsening dynamics for different shaker amplitudes is missing. Here, we address the following questions: (i) why do deep quenches favour transient networks while shallow ones do not, and (ii) how does this influence the pathway toward maximum compaction?

The paper is organized as follows. Section 2 describes the experimental methods, followed by the presentation of results in Section 3 and their discussion in Section 4. Summary and outlook are provided in Section 5.

2 Experimental methods

We describe the experimental setup (Section 2.1), the properties of the utilized spheres (Section 2.2), the measurement protocol (Section 2.3), and the image processing (Section 2.4).

2.1 Experimental setup

The experimental setup is sketched in Fig. 2. A rectangular vessel is filled with steel and glass beads with a diameter of 3 and 4 mm, respectively. The vessel (width × length × height = 200 × 285 × 20 mm^3) is made from a lightweight but stiff aluminum plate[34] supporting a glass plate and a plastic frame. An electroluminescent sheet (Zigan Displays) beneath the glass plate serves to illuminate the ferrogranulate from below. The vessel is closed from above by a rectangular box, having in the x and y directions the dimensions of the vessel, but with a height of 210 mm. The box is made of aluminum with a glass plate at the top. The box serves to contain the jumping spheres and to maintain an atmosphere of regulated humidity above 80% to steer clear of electrostatic charges.[41] Therefore, the box is connected by means of two pipes (d = 36 mm) and a fan to a tank partly filled with water, which harbors an ultrasonic transducer at its bottom. The transducer is connected *via* a relay to an adjustable AC source (EA-3048, 50 Hz). A humidity sensor inside the climate box[42] is connected *via* a microprocessor[43] and a USB-C cable to the computer. A python script maintains by means of a threshold-value-control a relative humidity in between 80% and 85%.

The humidity box is fixed to a rectangular frame,[44] whereas the vessel is agitated sinusoidally by an electromagnetic shaker.

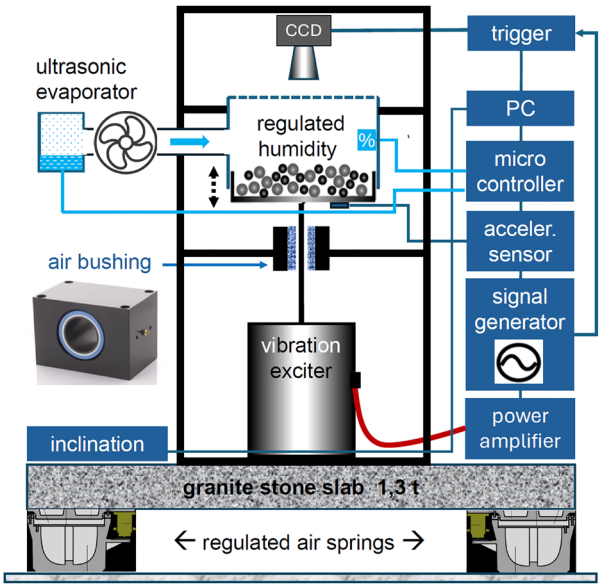

Fig. 2 A sketch of the experimental setup (not to scale). For details of the devices see text.

The narrow gap in between the vessel and the box is sealed by a 160 μm thin rubber bellow.[45]

The electromagnetic shaker (Tira Vib Co., TV50350) has been equipped with a compensation coil,[46] which reduces the stray field, as shown by the green line in Fig. 3. Moreover, the experimental vessel is mounted on top of a 480 mm long rod made from aluminum and brass, far away from the shaker. The brass section is guided friction-free by a porous media air bushing (NewWay S304002) with an inner diameter of 40.00 mm. In this way, the stray field could be reduced below a value of 0.12 mT.

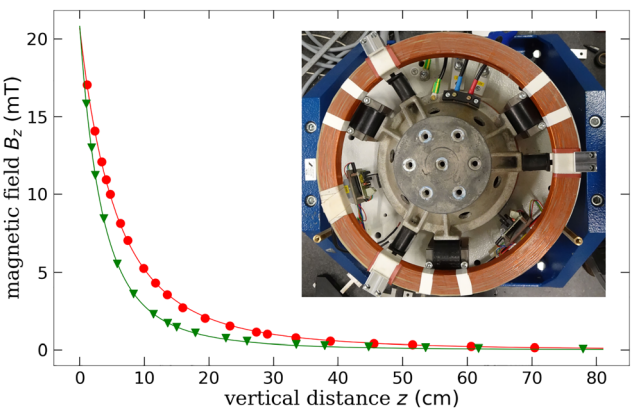

Fig. 3 The vertical component of the magnetic stray field of the vibration exciter (red data points) *vs.* the vertical distance z from the center of the top flange, *i.e.* the central plate with 7 holes in the inset photo. The green data points give the reduced stray field, when utilizing the compensation coils of the manufacturer (*cf.* inset). The lines indicate the corresponding fits by $B_z(z) = \mu_0\mu_S(2\pi)^{-1}(z_0 + z)^{-3}$, where the (compensated) magnetic dipole moment of the shaker is μ_S = 5.14 × 10^2(1.22 × 10^2) A m^2 and z_0 = 1.7 × 10^{-1}(1.05 × 10^{-1}) m, respectively.

The shaker is agitated sinusoidally, where frequency f and amplitude A are controlled by a function generator (Agilent FG33220) connected to a current amplifier (Tira Vib Co.). The non-dimensional acceleration $\Gamma = a/g_{\mathrm{loc}} = 4\pi^2 f^2 A/g$, with maximum acceleration a, shaking amplitude A, is monitored by an accelerometer (Dyson 3035B2). Here g_{loc} denotes the local gravitational acceleration 9.80961 m s^{-2} estimated by a standard model.[47] The air bearing and the shaker are mounted on a rectangular frame.[44]

A horizontal alignment of the experimental vessel is of utmost importance to allow drift-free long-term measurements. Likewise, the oscillating motion in the setup must be decoupled from the building. Therefore, the whole setup has been mounted on top of a granite stone slab (xyz = 1790 × 1290 × 152 mm^3) with a mass of 1.3 t, which is floating on four regulated air springs (Bilz BiAir 1-ED-AL-E), maintaining a vertical position with a precision of 10 μm. An inclinometer (Flex$^{\mathrm{TM}}$ H6MM of Rieker inc.) with a resolution of 0.05° serves to surveil the horizontal alignment. Recording the inclination for 18 h under load yields a deviation of less than 0.005°. Shaker, air bushing, and air springs are connected *via* a filter to pressurized air.

2.2 Spheres

In order to improve the thermal coupling between the shaken vessel and the clustering magnetized spheres we mix the latter with glass spheres.[31] The filling fraction ϕ of both types of spheres is defined *via*

$$\phi = N\frac{A_{\mathrm{hex}}}{A_{\mathrm{vessel}}} = N\frac{2\sqrt{3}r_{\mathrm{sphere}}{}^2}{A_{\mathrm{vessel}}}, \qquad (1)$$

where N counts the number of spheres, A_{hex} captures the area of the regular hexagon around a sphere of radius r_{sphere}, and $A_{\mathrm{vessel}} = 5.7 \times 10^4$ mm^2. In this way ϕ becomes 1 for a hexagonal close packing in 2D.[30,48] For all measurements reported here we selected N_{g} = 473 glass spheres and N_{s} = 841 steel spheres, which yields for both types of spheres an area filling factor of $\phi_{\mathrm{g}} = \phi_{\mathrm{s}} = 0.115$. To improve the tracking of the glass beads we selected transparent blue spheres displayed in Fig. 4. Previous to a series of measurements, the steel spheres are placed in a hexagonal grid maintained by a holder and magnetized by an induction of 1000 mT.[38] Their remanent moment m_{R} is determined using a vibrating sample magnetometer (Lakeshore, 7404).[34] It saturates for $B > 500$ mT, as shown in the IRM curve in Fig. 5. The inset displays the angular dependence of the impressed dipole moment, described by a harmonic function. The properties of both sphere types are listed in Table 1.

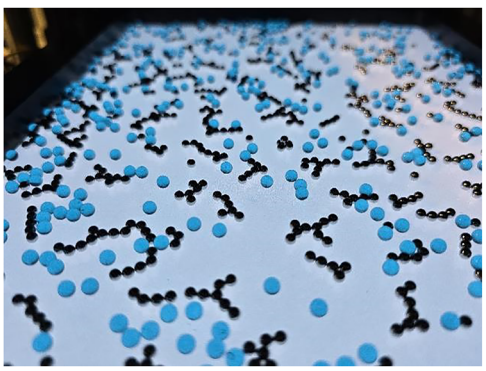

Fig. 4 A photo of the glass spheres (blue) and steel spheres (dark).

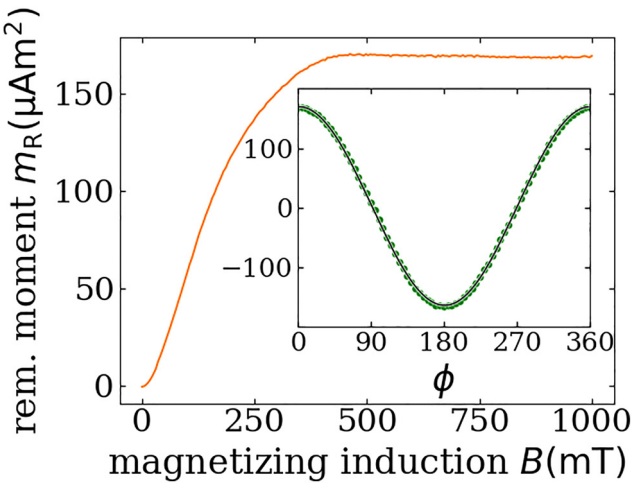

Fig. 5 The isothermal remanent magnetisation curve (IRM) of the utilized steel spheres. The inset displays the measured angular dependence of m_{R} magnetized with 1000 mT. The data are marked by green circles. The black line gives a fit by $m_0 \cos(\phi + \phi_0) + m_1$, with m_0 = 167.1 μA m^2, m_1 = 2.7 μA m^2, and $\phi_0 = -1.27°$.

Table 1 Material properties of the utilized spheres

Material	Steel	Glass
Supplier	ISOMetall	Sigmund Lindner
Type	DIN 1.3505 G10[32]	SiLibeads P* (blue)[33]
Radius (mm)	1.5	2.0
Precision (μm)	±9.75	±20
Mass (g)	0.108	0.084
Remanent moment m_{R} (10^{-6} A m^2)	173	—

2.3 Measurement protocol

Every set of measurements is conducted following this protocol. First, the acceleration amplitude is switched at $t = -15$ s to $\Gamma_{\mathrm{gas}} = 3.3$ g, which is ample time to generate a homogeneous granular gas. At $t = 0$ s the shaker amplitude is quenched to a value $\Gamma_n < \Gamma_{\mathrm{gas}}$, with $\Gamma_n \in [1.49, 2.02]$ g (*cf.* Table 2, Section A). The evolution of the pattern is recorded with 60 frames per second, in phase with the driving. With the internal storage capacity of the camera this allows a continuous recording for 180 s. Likewise, the shaker amplitude, the temperature, and the humidity in the experimental vessel are recorded. Then Γ is switched back to Γ_{gas}, then to a new value of Γ. The measurements for 8 consecutive values of Γ are repeated 15 times, in this way allowing to estimate a mean value and a standard deviation.

2.4 Image processing and data extraction

The granular patterns are observed from above using the charge-coupled device (CCD) camera Lumenera Lt425M. We

select a resolution of 1888 pixel × 1328 pixel. A multipulse generator allows triggering the camera in phase with the driving.[49] Two gray value intervals are preselected to discriminate between the blue glass spheres [185,220] and the opaque steel spheres [220,255]. In order to be able to analyze the networks of steel spheres, we apply the following image processing and data extraction procedure to the recorded frames. First, a Hough-transformation is applied to the images, followed by a binarization. These binary images are then processed with tools from the computer vision software OpenCV[50] which yields the contour and coordinates of the spheres. Next, for the identification of the networks, neighboring spheres have to be recognized. In order to do this, the center-to-center distance of each pair of spheres is compared with their diameter, $2r_{\mathrm{sphere}}$. The topology of the networks is reduced to a graph (see, *e.g.* Fig. 13 of ref. 34) by means of the software package networkX[51] based on the script language python.[52]

3 Experimental results

First we observe the evolution of the networks and clusters by naked eye (Section 3.1). This is followed by inspecting the number of neighbours *versus* time (Section 3.2), with special focus on the fraction of beads within chains (Section 3.3). Next, the stability of the emerging structures is derived from spectra displaying the fraction of nodes of a specific degree *versus* the shaking amplitude (Section 3.4). Then, combining Sections 3.2–3.4, a configuration diagram is extracted, which maps the predominant state (gas-like, networks or compact clusters) in the Γ–t plane (Section 3.5). Finally the mean number of neighbours $\bar{k}(t)$ (Section 3.6) as well as the half-value period (Section 3.7) of the growth dynamics is presented.

3.1 Evolution of the structures

Fig. 6 displays an overview of the evolution of the structures of magnetized spheres for three selected times after the quench (left to right: t_1 = 5 s, t_2 = 30 s, t_3 = 150 s) and for three representative shaker amplitudes (top to bottom: Γ_2 = 1.57 g, Γ_4 = 1.73 g, and Γ_6 = 1.88 g). For a quench to a very low amplitude (Γ_2), we observe emerging chains and rings already 5 s after the quench, which have developed to larger networks at 30 s, and become even more compact at 150 s. For intermediate shaking amplitude (Γ_4) clusters emerge later, and appear at 150 s to be more compact. After a shallow quench to a comparatively high amplitude (Γ_6), the granular gas persists for a long time. Likewise, networks are not seen, and clusters emerge only late at 150 s. They are even more compact than those at Γ_4. For even higher shaker amplitudes, clusters form even later (here not shown). Next, we will inspect the cluster formation by means of network quantities.

3.2 Number of neighbours *versus* time

The topology of the clusters formed by the magnetic beads can be represented as a network or a graph, in which each bead corresponds to a node or vertex, and the close contact

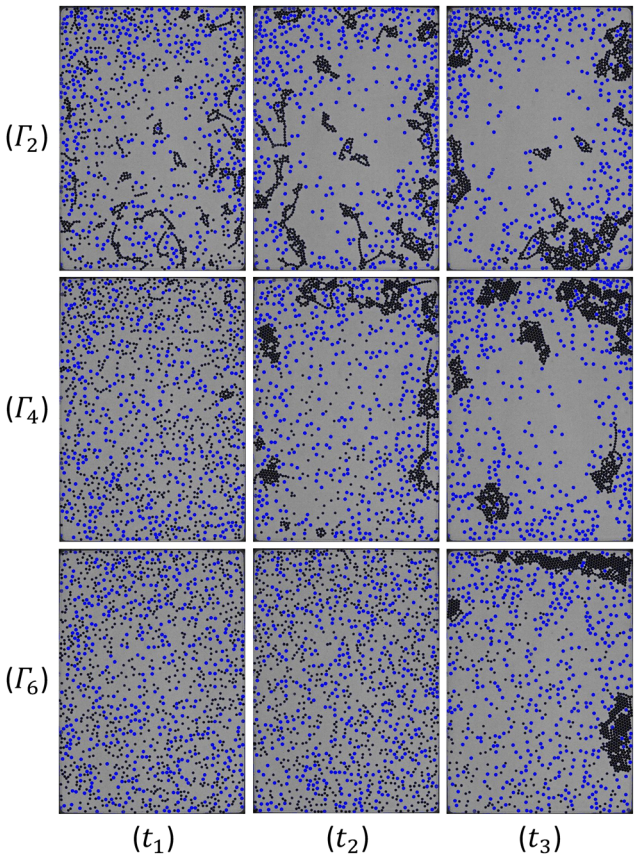

Fig. 6 Emerging structures for a quench from Γ_{gas} = 3.3 g down to increasing shaker amplitudes, Γ_2 = 1.57 g, Γ_4 = 1.73 g, and Γ_6 = 1.88 g. We display the structures for three exemplary times, namely t_1 = 5 s, t_2 = 30 s, and t_3 = 150 s. See also the related movies, 1.57g.mp4, 1.73g.mp4 and 1.88g.mp4, which can be accessed under "files" at https://doi.org/10.17605/OSF.IO/6S4FM.

connections between pairs of beads are represented by edges. Thus, in this description, the number of edges of each node – often addressed as its degree, k – represents the number of neighbours of the corresponding bead. A fundamental property of a network is its distribution of degrees, which in our case can help to identify the dominant structures in the system. In a chain-like structure, the beads have two neighbours, k = 2, except those at the chain ends, which have only one, k = 1. In a monodisperse two-dimensional system, k is limited geometrically to 6, corresponding to a hexagonal close packing. In the following, we define the fraction of nodes with degree k, F_k, as

$$F_k = \frac{n_k}{N_{\mathrm{S}}}, \quad k = \{0, 1, \ldots, 6\}, \tag{2}$$

where n_k is the number of steel spheres with k neighbours and N_{S} is the total number of steel spheres in the system. Thus, this parameter represents the probability of a magnetic bead to have a number of neighbours k.

In Fig. 7, we have plotted $F_k(t)$ for the three representative shaker amplitudes, illustrated in Fig. 6 above. In Fig. 7(a) the data for Γ_2 are plotted. Here the fraction of zero nodes F_0 (blue circles) drops drastically within 4.4 s to its half value.

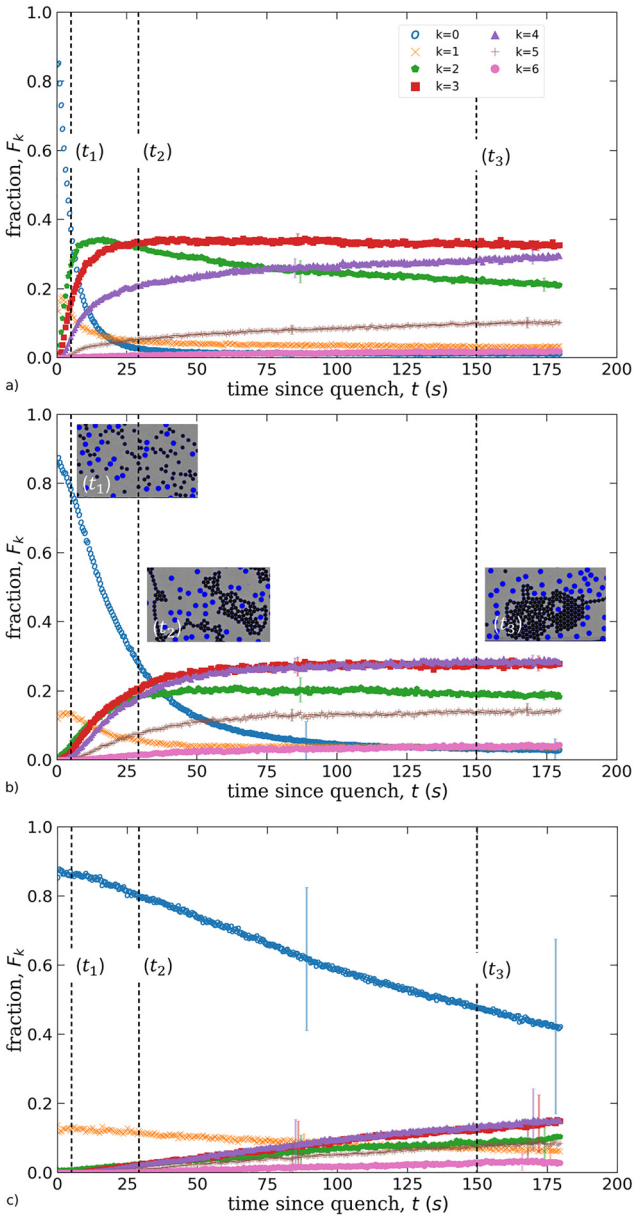

Fig. 7 Time evolution of F_k (2). The shaking amplitude Γ is kept constant in each run, but increases from Γ_2 (a) *via* Γ_4 (b) to Γ_6 (c). The legend in panel (a) applies to the three plots. The dashed vertical lines indicate to the times where the exemplary snapshots of Fig. 6 have been recorded. The insets in panel (b) display further cartoons for a gas-like state (t_1), a network-state (t_2) and a more compact cluster (t_3). All data points have been averaged from 15 subsequent runs. Representative error bars indicate the standard deviation.[53]

Simultaneously F_2 and F_3, characteristic for chains and Y-junctions, respectively, show a steep increase. That is, within a short time span of 14 s F_2 climbs to a maximum, and we witness the formation of networks. For larger times F_4 and F_5 is monotonic increasing, whereas F_2 and F_3 decay. This is indicating a coarsening of the network to more compact clusters, albeit on a much slower time scale.

The temporal evolution for Γ_4 is qualitatively different, as evidenced by Fig. 7(b). Here, F_0 drops less steeply, and F_3 and F_4 lack a prominent maximum. They have for most times the same amount. This corroborates that for higher Γ, chain- and network formation are bypassed soon, and the formation of compact clusters starts earlier. For even higher amplitude, Γ_6, the fraction of single spheres, F_0, is dominating the full measurement time. Here, we are approaching the threshold of aggregation as the kinetic energy of the particles is getting higher than the familiar magnetic coupling energy E_{DD}, as given by eqn (10) in ref. 38. The error bars in Fig. 7 indicate the standard deviation of 15 independent measurements. To retain clarity, we show only two representative examples in a run – one in the middle and one near the end. Note that the error bars are small in panel (a), but increase with the shaker amplitude (c). They are most prominent for F_0.

3.3 Fraction of nodes within chains, F_2

The emerging networks are made up from long chains, interconnecting at the ends. Therefore F_2 is a suitable order parameter to monitor generation and decay of networks. In Fig. 8 we give an overview of the temporal evolution of F_2 for all applied shaker amplitudes Γ. It shows that for a deep quench Γ_1, we see a fast build-up of chains and networks, which are then diminished on a much longer time scale. With Γ approaching Γ_4, the maximum of $F_2(t)$ becomes less prominent, and vanishes for $\Gamma > \Gamma_4$.

For a quantitative characterisation of Fig. 8 we resort to the bi-sigmoidal (i = 1, 2) growth function[54–56]

$$A(t) = A_{\mathrm{ini}} + \sum_{i=1}^{N=2} A_{\mathrm{gro},i}\left(1 - \frac{1}{1+\left(\frac{t}{t_{1/2,i}}\right)^{p_i}}\right) \qquad (3)$$

of a time dependent quantity A. Here A_{ini} denotes an offset, already present at $t < 0$ s and the maximal growth (or decay) is denoted by $A_{\mathrm{gro},i}$. The half-value period $t_{1/2,i}$ is the time when

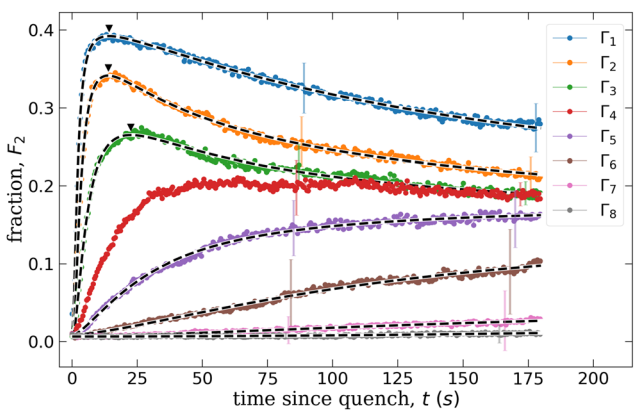

Fig. 8 Temporal evolution of F_2 for different applied shaking amplitudes Γ_i, as listed in Table 2, Section A. For clarity, only every fifth data point is plotted. The dashed lines represent fits by the bi-sigmoidal growth function (3). The fitting parameters are listed in Table 2. The black triangles (▼) mark the maximum determined from the fits for Γ_1, Γ_2, Γ_3, situated at 14.1 s, 13.8 s, and 22.5 s, respectively. All data points and representative error bars have been estimated from 15 independent measurements.[53]

$A = A_{ini} + A_{gro,i}/2$, and p_i is a scaling exponent that captures the curvature of the graph. For $N = 1$ and $A_{gro,1} > 0$ only one growth term is present. With $N = 2$ the growth function is bi-sigmoidal. For $A_{gro,2} > 0$, a further growth with a different rate may be captured (*c.f.* ref. 38), whereas for $A_{gro,2} < 0$ a subsequent decay can be described.

The dashed lines in Fig. 8 represent fits of $F_2(t,\Gamma)$ by eqn (3). The fitting values, listed in Table 2, Section A, clearly unveil the two different half-value times $t_{1/2,1}$ and $t_{1/2,2}$, needed to fit $\Gamma_{1,2,3}$. The first reflect the emergence, and the second the decay of the networks in favour of more compact clusters. At Γ_1 we find a big difference of 142 s between both times. This difference is diminishing monotonously with Γ, until for $\Gamma_5,\ldots,\Gamma_8$ only one time scale is left, capturing the monotonic growth of F_2. Obviously injecting more kinetic energy into the system facilitates the direct arrangement of compact clusters, whereas the the head-to-tail assembly of magnetized beads is bypassed.

3.4 Number of neighbours *versus* shaking amplitude

In the previous sections, we have inspected the fraction of nodes F_k in their temporal evolution to characterize the coarsening dynamics from ferrogranular gas *via* transient networks to compact clusters. This temporal direction suggests that compact clusters exhibit greater stability compared to networks or chains.

An insight into the relative stability of different structures can be gained from a plot of the F_k-spectrum *vs.* Γ, as shown in Fig. 9 at $t = 180$ s. For clarity, we have plotted in panel (a) F_0, F_1, F_2 only, and in panel (b) the remainder. Panel (a) reveals a steep increase of the fraction of single particles, F_0, for $\Gamma > 1.8$ g, whereas F_2 (steel beads within chains) drops around that amplitude. In contrast, chain ends or dimers, F_1, are few for all Γ, indicating that if chains are formed they are rather long.

The spectrum of $F_k(\Gamma)$ is quite different for $k = 3\ldots6$. Here, the compact structures, captured by $F_{5,6}$ have a maximum at $\Gamma = 1.8$ g and basically fully disappear at higher amplitudes. On the other hand, structures characterized by F_4 that are not as compact exhibit reduced stability, reaching a peak already at 1.65 g and then gradually disappear. It is important to mention that Y-branches within networks, represented by F_3, monotonously diminish as Γ increases.

Of course, Fig. 9 can give only an instantaneous image at $t = 180$ s. For earlier times see the related movies to Fig. 9(a)[57] and (b).[58] They display the spectra $F_k(\Gamma, t)$ in their temporal evolution. In the first movie[57] $F_{0,1,2}(\Gamma, t)$ is starting from equipartition, where $F_0 \approx 0.9$ dominates. Around $t = 30$ s, the step-like increase of $F_0(\Gamma)$ becomes prominent, and remains stable for later times, but is slightly shifted to higher Γ. Likewise, the second movie[58] unveils how $F_{3,4,5,6}(\Gamma)$ are rising from zero and are developing first maxima already at $t \approx 15$ s. As time goes by, these maxima are shifted to higher values of Γ.

3.5 Configuration diagram

For a condensed overview of the three ferrogranular configurations we coarse grain the measured fraction of nodes as follows. The gas-like state is clearly captured by F_0. The networks

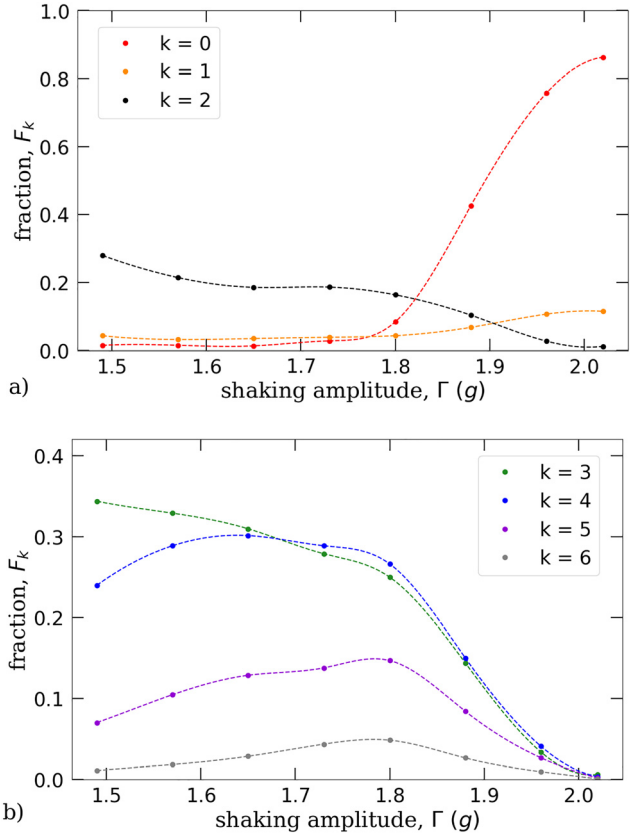

Fig. 9 Relative fraction of nodes *vs.* the shaking amplitude at $t = 180$ s. Panel (a) displays $k = 0, 1, 2$, panel (b) $k = 3,\ldots,6$. The dashed lines are splines to guide the eye. A movie displaying the temporal evolution of $F_k(\Gamma)$ can be accessed at https://doi.org/10.17605/OSF.IO/6S4FM. All data points are averaged over 15 independent measurements. For error bars see Fig. 7.

comprise chain ends, chains and branching sites and may thus be characterized by $F_{1,2,3} = F_1 + F_2 + F_3$. The more compact cluster are summarized by $F_{4,5,6} = F_4 + F_5 + F_6$. The resulting configuration diagram is shown in Fig. 10. To facilitate a clear division the regimes where the gas configuration ($F_0 > 2/3$), or the network configuration ($F_{1,2,3} > 2/3$) prevail have been plotted in colour. The remainder indicates in grey the fraction of the clusters.

The configuration diagram corroborates, that for a quench to a high shaking amplitude the gas-like state (F_0) persists for most of the observation time (marked in red/yellow). In contrast, at low Γ, transient networks (marked in shades of blue) exists only for a short time, and give soon way to more compact clusters, characterized by the grey area. Most importantly, quenching to an intermediate level of Γ allows to bypass the network configuration.

3.6 Mean number of neighbours

What drives the coarsening dynamics from networks towards more compact clusters? As pointed out in the introduction, the susceptibility of the magnetized spheres is a main ingredient. In compact clusters, the magnetic stray fields may be reduced, and with it the magnetic field energy.

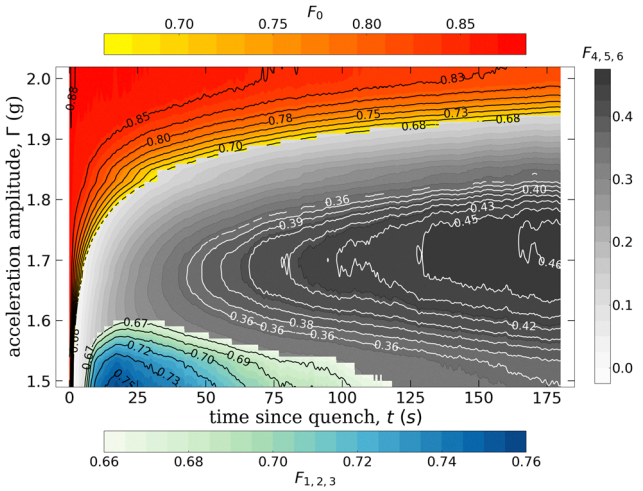

Fig. 10 Configuration diagram of three different ferrogranular states, that are gas-like (F_0), networks ($F_{1,2,3} = F_1 + F_2 + F_3$), and compact clusters ($F_{4,5,6} = F_4 + F_5 + F_6$). For a condensed overview the regimes where $F_0 > 2/3$ and $F_{1,2,3} > 2/3$ have been plotted in colour, and $F_{4,5,6}$ in the remainder in grey. The related colour codes are indicated at the top, bottom, and at r.h.s. To improve the resolution in Γ the splines of Fig. 9 have been utilized to estimate the different fractions.

A suitable order parameter for the network evolution to more compact structures is the mean number of neighbours, $\bar{k}$, that is defined as

$$\bar{k} = \frac{\sum_{k=0}^{6} k n_k}{N_S} = \sum_{k=0}^{6} k F_k. \quad (4)$$

The evolution of $\bar{k}(t, \Gamma)$ is plotted in Fig. 11. It displays for all Γ a monotonic increase. Consistent with the observations for F_k, for minimal shaker amplitude, Γ_1, (blue circles) one can discriminate between two regimes. In the first regime, which lasts about 25 s, we observe a fast increase of $\bar{k}$, that is correlated with the formation of chains and networks, as characterized by F_2 in Fig. 8. After that, the clusters evolve to form more compact structures, making $\bar{k}$ increase on a much longer time scale.

Those two regimes have different time scales, but are part of a common coarsening process. Indeed, the temporal evolution of $\bar{k}$ can well be fitted by a common function for both regimes. It is the sigmoidal growth function

$$\bar{k}(t) = \bar{k}_{\mathrm{ini}} + \bar{k}_{\mathrm{gro}} \left(1 - \frac{1}{1 + \left(\frac{t}{t_{1/2}} \right)^p} \right), \quad (5)$$

that describes diverse limited growth processes in nature,[54,55] and is a basic version of eqn (3). Here, $\bar{k}_{\mathrm{ini}}$ denotes an offset, already present at $t < 0$ s, which characterizes short time contacts during the collisions of spheres. The maximal growth is marked by $\bar{k}_{\mathrm{gro}}$. Moreover, $t_{1/2}$ denotes the half-value period when $\bar{k}(t_{1/2}) = \bar{k}_{\mathrm{ini}} + \bar{k}_{\mathrm{gro}}/2$, and p is a scaling exponent, which captures the curvature of the graph. The fitting parameters are listed in Table 2 in Section A. Note that $\bar{k}_{\mathrm{ini}}$ and $\bar{k}_{\mathrm{gro}}$ have close

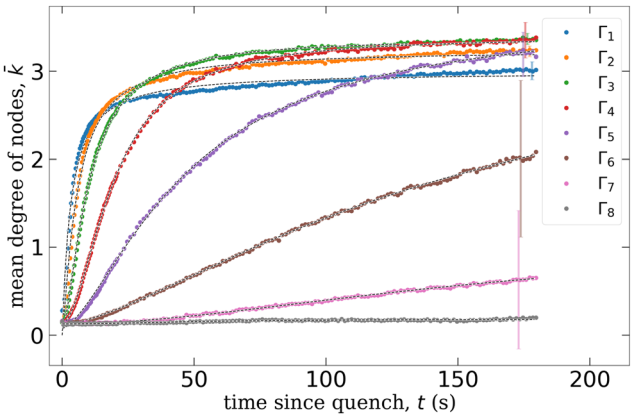

Fig. 11 Temporal evolution of the mean degree of the nodes for different applied shaking amplitudes, as listed in Table 2 (Section A). To not overload the graphs, for $t < 4$ s every 5th data point has been plotted, and for $t > 4$ s only every 15th data point has been plotted. The dashed lines mark fits by eqn (5). All data points and representative error bars have been estimated from 15 independent measurements.[53]

values for $\Gamma_1 \ldots \Gamma_6$. Only for Γ_7 and Γ_8 the gradual increase does not provide enough data for a reliable fit.

We stress that Fig. 11 reconfirms our previous observation in Fig. 8 and 10. Transient network formation occurs on a fast track. The sharp increase of $F_2(t)$ is contributing to the rapid rise of $\bar{k}(t)$. With increasing Γ network formation is fading, and the fast increase of $\bar{k}(t)$ vanishes, but the slow one remains.

3.7 Half-value period

A convenient observable to grasp the retardation of the network evolution in both regimes is the half-value period $t_{1/2}(\Gamma)$, as given in column 5 of Table 2 (Section A). It is plotted in Fig. 12 by blue circles. The first slow, then rapid increase of $t_{1/2}(\Gamma)$ can well be described by an exponential function

$$t_{1/2}(\Gamma) = t_1 \exp\left(\frac{\Gamma}{\Gamma_e} \right) + t_2. \quad (6)$$

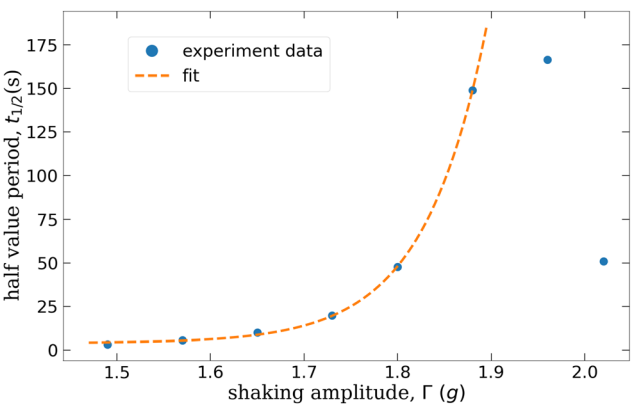

Fig. 12 Half-value period *versus* shaking amplitude. The dashed line indicates a fit by eqn (6), where only the data [Γ_1, Γ_6] are taken into account. Fitting parameters are $t_1 = (1.06 \times 10^{-10} \pm 6.6 \times 10^{-11})$ s, $\Gamma_e = (6.7 \times 10^{-2} \pm 1.5 \times 10^{-3})$ g and the offset $t_2 = (4.02 \pm 6.7 \times 10^{-1})$ s.

The fitting parameters are given below Fig. 12. Note that the values for $\Gamma_{7,8}$ are not captured by eqn (6). One reason may be that an insufficient part of the growth process has been recorded during the measurement time.

4 Discussion

The configuration diagram in Fig. 10 summarizes our experimental findings. Following a deep quench in the shaking amplitude Γ, we observe an ''island of networks'' (shades of blue), whereas for intermediate amplitudes ($\Gamma \approx 1.7$ g) compact clusters form immediately (shades of grey). This ''island of networks'' has major implications for the coarsening dynamics leading to optimally compact clusters. As indicated by the dark-shaded area in Fig. 10, the most compact states occur around $(t, \Gamma) \approx$ (180 s, 1.7 g). Strikingly, at lower Γ—and thus lower granular temperature—the one sees an anomalous trend: further cooling reduces compaction. This behaviour is evident in the $\bar{k}(t, \Gamma)$ diagram in Fig. 11, which displays a non-monotonic dependence of $\bar{k}$ in the advanced coarsening regime.[59] Correspondingly, the growth rate k_{gro} increases transiently with Γ (see Table 3, Section A).

Such non-monotonic behaviour was absent in previous studies, where coarsening dynamics were tuned by an external magnetic induction B_z.[38,60] A comparison between $\bar{k}(t, B_z)$ curves at fixed Γ (see Fig. 7 in ref. 38) and the $\bar{k}(t, \Gamma)$ curves shown in Fig. 11 reveals a similar overall trend. Even the fitted parameters in Table 3 are related, with comparable scaling exponents p.[61] However, magnetically controlled coarsening lacks anomalous compaction: each $\bar{k}(t,B_z)$ curve at lower induction serves as an envelope for those at higher B_z. The deterministic magnetic torque $\vec{m}_R \times \vec{B}_z$ (Zeeman coupling) suppresses head-to-tail alignment in a monotonic fashion,[62] whereas variations in Γ produce a non-monotonic response with multiple effects discussed below.

Our results indicate the presence of two distinct time scales that govern the structural evolution of the system. On short time scales, chains and networks form rapidly (Fig. 8), while on longer time scales these structures evolve into compact clusters. In contrast, after a shallow quench in Γ, both F_2 (Fig. 8) and $\bar{k}$ (Fig. 11) show only gradual cluster formation over an extended period. The emergence of two characteristic time scales thus appears inherently linked to the transient-network regime.

Previous studies have suggested that coarsening in such systems arises from the dynamic asymmetry between magnetized and non-magnetic (glass) beads.[34,38] However, this cannot account for the absence of networks after shallow quenches. We therefore propose that two intrinsic time scales exist within a single constituent the steel beads themselves. For deep quenches, where $E_{kin} < E_{DD}$ (the dipole–dipole coupling energy), dipolar interactions dominate, leading to rapid head-to-tail chain and network formation. The dipolar hard-sphere (DHS) characteristics drive the initial network stage, while the additional magnetic susceptibility of the beads governs the later coarsening phase. Thus, both dipolar (''D'') and susceptible (''S'') properties of the susceptible dipolar hard spheres (SDHS) are manifest, but on different time scales. At higher Γ, additional energy input counteracts magnetic dipolar interactions E_{DD}, suppressing the fast network-forming time scale. Increased mobility promotes greater compaction, yet excessive kinetic energy lowers the probability of a magnetic attachment, leading to an exponential increase of the half-value time, as shown in Fig. 12.

5 Summary and outlook

We have measured the response of a mixture of glass and magnetized steel beads after the shaking amplitude is suddenly quenched from a high value, $\Gamma_{gas} = 3.3$ g (homogeneous gas phase), to a lower value (separated phase). For a deep quench to $\Gamma \approx 1.5$ g, we observe the rapid formation of chains and networks, which subsequently and slowly coarsen into compact clusters. In contrast, for a shallow quench to $\Gamma \approx 1.7$ g, we record the direct and gradual assembly of compact clusters, without an intermediate network phase.

To quantify these coarsening dynamics, we employ network order parameters such as the fraction of nodes F_k of order k. Especially F_2 turned out to be a suitable observable to monitor the emergence and decay of transient networks. It can be fitted by means of a bi-sigmoidal growth function (3) which yields two distinct half-value-times – a short one ($\simeq 2$ s) for the generation of networks and a long one ($\simeq 144$ s) mirroring their transformation into compact clusters. For higher shaking amplitude transient networks are fading, and the two characteristic times approach, until only one time scale remains ($\Gamma > 1.7$ g). This threshold may be situated at the dipole–dipole coupling energy, which is overcome by the kinetic energy. A measure characterizing the over-all coarsening dynamics is the mean number of neighbours $\bar{k}$. Here, across the range of quench amplitudes Γ, the transition between network-mediated and direct clustering regimes is continuous and well described by a plain sigmoidal growth function (5) for $\bar{k}(t, \Gamma)$. The half-value-time $t_{1/2}$ of this function increases exponentially with Γ. Despite that, $\bar{k}$ reaches a relative maximum for $\Gamma \approx 1.7$ g, $t = 180$ s. This path to maximal compaction may be of interest for packing theory.[63–65]

The emergence of two distinct time scales – an initial rapid assembly and a slower coarsening – appears to be an intrinsic property of a ferrogranulate composed of susceptible dipolar hard spheres (SDHS). The initial network formation is driven by dipolar interactions, while the slower transition to compact clusters is governed by the magnetic susceptibility. Importantly, these two processes emerge from different physical properties of the same constituent particles. This behaviour resembles viscoelastic phase separation,[66] where, however, the necessary time-scale separation originates from compositional diversity. In the ferrogranulate, the time-scale separation may originate from internal magnetic complexity. Therefore, we conjecture that a pure ferrogranulate – without glass beads – would also exhibit transient network formation, driven by the

same dipolar interactions. While the current system includes non-magnetic glass beads, which influence collision dynamics and the final packing, we anticipate that the essential features of the two-stage assembly process are preserved. The experimentum crucis to isolate these effects – measuring with a ferrogranulate without glass spheres – remains yet to be performed.

Author contributions

Ali Lakkis: assembling the setup, performing the measurements, data curation, visualization, formal analysis, software; Matthias Biersack: construction of the humidity regulation loop, design and implementation of the related software, validation; Oksana Bilous: writing – review & editing; Sofia Kantorovich: writing – review & editing, funding acquisition; Reinhard Richter: conceptualization of the study and setup, assembling, methodology, measuring the magnetization, writing – original draft, funding acquisition, supervision.

Conflicts of interest

There are no conflicts to declare.

Data availability

All processed data which have been plotted in the figures, can be accessed at https://doi.org/10.17605/OSF.IO/6S4FM. Moreover, the reader will find there as well a selection of primary data in the form of movies. More primary data may be obtained upon request from the corresponding authors.

Supplementary information: Movies of the coarsening dynamics for 3 exemplary acceleration amplitudes, movies for the temporal evolution of Fig. 9, and processed experimental data of all plots can be found at https://doi.org/10.17605/OSF.IO/6S4FM. See DOI: https://doi.org/10.1039/d5sm00726g.

Appendix

A Appendix

Tables 2 and 3.

Table 2 The table displays the utilized acceleration amplitudes Γ_n. A fit of eqn (3) to the data for the fraction $F_2 \equiv A$ as displayed in Fig. 8, yields the parameters displayed in columns 3 to 9. Note that at the transitional acceleration Γ_4 the fit has a large scatter and is therefore not listed

Γ_n	(g)	$F_{2,\mathrm{ini}}$	$F_{2,\mathrm{gro},1}$	$t_{1/2,1}$ (s)	p_1	$F_{2,\mathrm{gro},2}$	$t_{1/2,2}$ (s)	p_2
Γ_1	1.49	0.015	0.40	2.06	2.00	−0.25	144.21	1.21
Γ_2	1.57	0.010	0.50	3.36	1.75	−0.38	33.93	0.74
Γ_3	1.65	0.008	0.50	6.29	1.51	−0.36	23.13	0.93
Γ_4	1.73	—	—	—	—	—	—	—
Γ_5	1.80	0.008	0.17	31.64	1.43	—	—	—
Γ_6	1.88	0.009	0.14	128.47	1.45	—	—	—
Γ_7	1.96	0.007	0.04	200.35	1.55	—	—	—
Γ_8	2.02	0.006	0.08	715.22	2.00	—	—	—

Table 3 The table displays the utilized acceleration amplitudes Γ_n. A fit of (5) to the data for the mean degree of a node $\bar{k}$, as displayed in Fig. 11, yields the parameters displayed in columns 3 to 6

Γ_n	(g)	$\bar{k}_{\mathrm{ini}}$	$\bar{k}_{\mathrm{gro}}$	$t_{1/2}$ (s)	p
Γ_1	1.49	0.10	2.90	3.59	1.06
Γ_2	1.57	0.10	3.12	6.12	1.28
Γ_3	1.65	0.10	3.27	10.45	1.55
Γ_4	1.73	0.15	3.24	20.73	1.85
Γ_5	1.80	0.10	3.60	50.68	1.54
Γ_6	1.88	0.12	3.18	148.91	1.47
Γ_7	1.96	0.13	0.90	165.23	1.86
Γ_8	2.02	0.13	0.05	51.26	1.99

Acknowledgements

The authors thank Klaus Oetter and the mechanical workshop of NW2 at the University of Bayreuth for their precise construction work. Moreover, we thank Peter Daxer (Bilz Vibration Technology AG) and Alexander Wölfel (Sigmund Lindner GmbH) for helpful advice. Fruitful discussions with Kai Huang, Arshad Kudrolli, Pedro A. Sánchez, Matthias Schröter and Simeon Völkl are gratefully acknowledged. In addition we acknowledge deep questions of three anonymous referees. Last but not least, we thank Oliver Bäumchen for lab space. The research was supported by the German-Austrian (D–A) ferrogranular research project funded by DFG (Ri 1054/7) and FWF (I5160).

Notes and references

1 N. V. Brilliantov and T. Pöschel, *Kinetic theory of granular gases*, Oxford University Press, USA, 2010.
2 J. Duran, *Sands, powders, and grains: an introduction to the physics of granular materials*, Springer Science & Business Media, 2012.
3 B. Andreotti, Y. Forterre and O. Pouliquen, *Granular media: between fluid and solid*, Cambridge University Press, 2013.
4 R. E. Rosensweig, *Ferrohydrodynamics*, Cambridge University Press, Cambridge, New York, Melbourne, 1985.
5 M. D. Cowley and R. E. Rosensweig, *J. Fluid Mech.*, 1967, **30**, 671.
6 R. Richter and A. Lange, Surface Instabilities of Ferrofluids, in *Colloidal Magnetic Fluids: Basics, Development and Applications of Ferrofluids*, Springer, Berlin, Heidelberg, New York, 2009, vol. 763, ch. 3, pp. 157–243.
7 D. Lopez and F. Pétrélis, *Phys. Rev. Lett.*, 2010, **104**, 158001.
8 M. Klokkenburg, R. Dullens, W. Kegel, B. Erne and A. Philipse, *Phys. Rev. Lett.*, 2006, **96**(037203), 1–4.
9 *Colloidal Magnetic Fluids: Basics, Development and Applications of Ferrofluids*, ed. S. Odenbach, Springer, Berlin, Heidelberg, New York, 2009, vol. 763.
10 T. A. Prokopieva, V. A. Danilov, S. S. Kantorovich and C. Holm, *Phys. Rev. E: Stat., Nonlinear, Soft Matter Phys.*, 2009, **80**, 031404.
11 S. Kantorovich, A. Ivanov, L. Rovigatti, J. Tavares and F. Sciortino, *Phys. Rev. Lett.*, 2013, **110**, 148306.

12 S. S. Kantorovich, A. O. Ivanov, L. Rovigatti, J. M. Tavares and F. Sciortino, *Phys. Chem. Chem. Phys.*, 2015, **17**, 16601–16608.
13 D. Vella and L. Mahadevan, *Am. J. Phys.*, 2005, **73**, 817–825.
14 A. Snezhko, I. S. Aranson and W. K. Kwok, *Phys. Rev. Lett.*, 2005, **94**, 108002.
15 R. Messina, L. A. Khalil and I. Stanković, *Phys. Rev. E: Stat., Nonlinear, Soft Matter Phys.*, 2014, **89**, 011202.
16 S. Egri and G. Bihari, *J. Phys. Commun.*, 2018, **2**, 105003.
17 E. Opsomer, S. Merminod, J. Schockmel, N. Vandewalle, M. Berhanu and E. Falcon, *Phys. Rev. E*, 2020, **102**, 042907.
18 J. Stambaugh, D. P. Lathrop, E. Ott and W. Losert, *Phys. Rev. E: Stat., Nonlinear, Soft Matter Phys.*, 2003, **68**, 026207.
19 J. Stambaugh, Z. Smith, E. Ott and W. Losert, *Phys. Rev. E: Stat., Nonlinear, Soft Matter Phys.*, 2004, **70**, 031304.
20 C. Laroche and F. Pétrélis, *Eur. Phys. J. B*, 2010, **77**, 489–492.
21 L. Oyarte, P. Gutiérrez, S. Aumatre and N. Mujica, *Phys. Rev. E: Stat., Nonlinear, Soft Matter Phys.*, 2013, **87**, 022204.
22 S. Boccaletti, V. Latora, Y. Moreno, M. Chavez and D.-U. Hwang, *Phys. Rep.*, 2006, **424**, 175–308.
23 W. Wen, F. Kun, S. Pal, D. Zheng and K. Tu, *Phys. Rev. E: Stat. Phys., Plasmas, Fluids, Relat. Interdiscip. Top.*, 1999, **59**, R4758.
24 N. Osterman, I. Poberaj, J. Dobnikar, D. Frenkel, P. Ziherl and D. Babić, *Phys. Rev. Lett.*, 2009, **103**, 228301.
25 F. J. Maier and T. M. Fischer, *Soft Matter*, 2015, **12**, 614–618.
26 F. J. Maier and T. M. Fischer, *J. Phys. Chem. B*, 2016, **120**, 10162–10165.
27 J. E. Martin and A. Snezhko, *Rep. Prog. Phys.*, 2013, **76**, 126601.
28 H. Carstensen, A. Krämer, V. Kapaklis and M. Wolff, *Soft Matter*, 2022, **18**, 6222–6228.
29 A. Snezhko, *Curr. Opin. Coll. Int. Sci.*, 2016, **21**, 65–75.
30 D. L. Blair and A. Kudrolli, *Phys. Rev. E: Stat., Nonlinear, Soft Matter Phys.*, 2003, **67**, 021302.
31 D. L. Blair and A. Kudrolli, in *The Physics of Granular Media*, ed. H. Hinrichsen and D. Wolf, Wiley-VCH Verlag GmbH & Co. KGaA Weinheim, FRG, 2004, ch. 12, pp. 281–296.
32 Isometall datasheet, steel balls out of 1.3505, https://www.isometall.de, https://www.isometall.de/downloads/Datenblatt-1.3505.pdfDatenblatt-1.3505.pdf.
33 Sigmund Lindner, https://www.sili.eu, https://www.sili.eu/wp-content/uploads/2018/08/SiLibeads_Type_P-1.pdfSiLibeads Type P.
34 A. Kögel, P. A. Sánchez, R. Maretzki, T. Dumont, E. S. Pyanzina, S. S. Kantorovich and R. Richter, *Soft Matter*, 2017, **14**, 1001–1015.
35 P. A. Sánchez, J. Miller, S. S. Kantorovich and R. Richter, *J. Magn. Magn. Mater.*, 2020, **499**, 166182.
36 A. Smolla, Bachelor thesis, Universität Bayreuth, Bayreuth, Germany, 2018.
37 A. Smolla, A. G. Sourais, S. S. Kantorovich, A. Boudouvis and R. Richter, *Force enhancement in-between susceptible dipolar hards spheres - measurement vs. computation*, manuscript, 2025.
38 M. Biersack, A. Lakkis, R. Richter, O. Bilous, P. A. Sánchez and S. S. Kantorovich, *Phys. Rev. E*, 2023, **108**, 054905.
39 W. H. Stockmayer, *Rev. Mod. Phys.*, 1959, **31**, 103–106.
40 A. Wafflard, E. Opsomer and N. Vandewalle, *Phys. Rev. E*, 2024, **110**, 054608.
41 A. Schella, S. Herminghaus and M. Schröter, *Soft Matter*, 2017, **13**, 394–401.
42 Tinkerforge Humidity Bricklet 2.0, HIH-5030/5031, resolution 0.01% RH.
43 Tinkerforge Masterbrick 3.2.
44 The frame with the dimensions width × depth × height = 935 × 103 × 155 mm3 is made of aluminum construction material of Paletti Co. The vertical bars are having a cross-section of 80 × 80 mm^2, horizontal bars one of 80 × 40 mm^2.
45 Russka Co., Theraband ''Yellow''.
46 Tira Vib Co., compensation coil, serial number 130/09 0160465.
47 The University of Bayreuth is situated in 338 m above see level at a latitude of 49.9478200°. Utilizing the https://www.ptb.de/cms/ptb/fachabteilungen/abt1/fb-11/fb-11-sis/g-extractor.htmlPTB-g-extractor yields a local gravitational acceleration of 9.80961 m/s.
48 Note that there is a typo in eqn (3) of ref. 34.
49 K. Huang and I. Rehberg, *Phys. Rev. Lett.*, 2011, **107**, 028001.
50 Open Computer Vision (openCV), https://github.com/opencv/opencv/wiki.
51 NetworkX: High-productivity software for complex networks, https://networkx.github.io/https://networkx.github.io/, link accessed at 4.5.2025.
52 *Python software foundation*, https://www.python.org/, accessed at the 4th of May 2025, 2025.
53 The error bars are slightly shifted in time to make them better distinguishable.
54 D. W. Thompson, *On Growth and Form*, Cambridge University Press, Cambridge, UK, 2nd edn, 1942.
55 A. Tsoularis and J. Wallace, *Math. Biosci.*, 2002, **179**, 21–55.
56 P. Meyer, *Technol. Forecast.*, 1994, **47**, 89–102.
57 A. Lakkis, *Movie Fkvsampk012.mp4*, https://osf.io/3acnj https://osf.io/3acnj, 2025, Online; accessed 4-May-2025.
58 A. Lakkis, *Movie Fkvsampk3456.mp4*, https://osf.io/j6m2y https://osf.io/j6m2y, 2025, Online; accessed 4-May-2025.
59 An increase of $\bar{k}(\Gamma)$ in the advanced coarsening regime has been reported in ref. 34 before. See the $\bar{k}(t)$-curves for two different shaking amplitudes in Fig. 15. Thus this effect is here validated in a wide range of Γ_i.
60 A. Lakkis, M. Biersack, O. Bilous, S. Kantorovich and R. Richter, *J. Magn. Magn. Mater.*, 2024, **589**, 171620.
61 Comparing the Table 3 we find small deviations: The throughout lower values for k_{ini} in our present measurements are a benefit of the presently more advanced setup and the faster frame rate. Likewise, the throughout higher values of k_{gro} are a consequence of a longer measuring time – 180 s instead of 120 s.
62 This interpretation is corroborated when comparing the spectrum $F_k(B)$ (Fig. 6 in ref. 38) to the spectrum $F_k(\Gamma)$, as shown in Fig. 8 above. In the magnetically controlled case, we note again a monotonic decay of $F_k > 2(B)$, whereas

$F_k > 2(\Gamma)$ displays maxima, before the clusters are dissolved.

63 I. Biazzo, F. Caltagirone, G. Parisi and F. Zamponi, *Phys. Rev. Lett.*, 2009, **102**, 195701.

64 H.-K. Chan, S. Hutzler, A. Mughal, C. S. O'Hern, Y. Wang and D. Weaire, *Packing Problems in Soft Matter Physics: Fundamentals and Applications*, Royal Society of Chemistry, 2025, vol. 27.

65 M. Schröter, D. I. Goldman and H. L. Swinney, Stationary state volume fluctuations in a granular medium, *Phys. Rev. E*, 2005, **71**, 030301.

66 H. Tanaka, *J. Phys.: Condens. Mater.*, 2000, **12**, R207.